





ARTICLE OPEN



Driving ultrafast spin and energy modulation in quantum well states via photo-induced electric fields

Samuel T. Ciocys^{1,2}, Nikola Maksimovic^{1,2}, James G. Analytis^{1,2} and Alessandra Lanzara^{1,2}

The future of modern optoelectronics and spintronic devices relies on our ability to control the spin and charge degrees of freedom at ultrafast timescales. Rashba spin-split quantum well states, 2D states that develop at the surface of strong spin-orbit coupling materials, are ideal given the tunability of their energy and spin states. So far, however, most studies have only demonstrated such control in a static way. In this study, we demonstrate control of the spin and energy degrees of freedom of surface quantum well states on Bi₂Se₃ at picosecond timescales. By means of a focused laser pulse, we modulate the band-bending, producing picosecond time-varying electric fields at the material's surface, thereby reversibly modulating the quantum well spectrum and Rashba effect. Moreover, we uncover a dynamic quasi-Fermi level, dependent on the Lifshitz transition of the second quantum well band bottom. These results open a pathway for light-driven spintronic devices with ultrafast switching of electronic phases, and offer the interesting prospect to extend this ultrafast photo-gating technique to a broader host of 2D materials.

npj Quantum Materials (2022)7:79; <https://doi.org/10.1038/s41535-022-00490-2>

INTRODUCTION

Quantum well (QW) states in semiconductors are a result of a confining potential that traps electrons (typically in a 2D plane) quantizing their electronic states. These states are easy to produce, have tunable band gaps, and are conceptually simple in terms of quantum systems. For these reasons, they have yielded a plethora of applications such as high-efficiency solar cells, infrared lasers, and qubits^{1–4}. Suitable confinement potentials can be achieved by constructing a multilayer heterostructure, but they can also occur spontaneously on surfaces from an adsorbate-induced localized surface potential^{5–7}. When these states appear on the surface, the breaking of inversion symmetry removes the spin-degeneracy resulting in spin-polarized QW states^{8–13}. Combining quantum confinement with strong spin-orbit coupling joins the malleable electronic dispersions of QW states with the robust spin-polarization of Rashba states, making them extremely promising candidates for spin-based devices, such as the Datta Das spin-transistor^{14,15}.

Since the Rashba interaction and QW spectrum are both predicated on the underlying electric potential, tuning the surface potential becomes a powerful method to manipulate both their spin and energy degrees of freedom^{7,16–18}. Such control has been achieved via in-situ surface chemical doping (irreversible and difficult to implement in devices)^{9,12,19,20} and electrostatic gating (ideal for devices but often limited by the magnitude of the QW potential at the surface of bulk samples, $10^7–10^{13}$ V m^{−1})^{21–23}. The real downfall of both methods is in the difficulty to dynamically tune the QW states on ultrafast timescales, restricting the ability to study the fundamental mechanisms of electronic relaxation and limiting device application in the time domain.

Here, by combining the surface photovoltage effect (SPV), a well-studied mechanism for producing reversible surface potentials in many semiconductors, with time and angle-resolved photoemission spectroscopy, we demonstrate an ultrafast and reversible control of Rashba splitting and energy level spacing, and subsequent quasi-equilibrium charge storage in


correspondence with a photo-induced Lifshitz transition. This is in contrast to proposed methods of spin-current manipulation in topological insulators using the SPV to solely change the local surface potential of the Dirac surface state^{24–26}. These results present an all-in-one approach for light-driven spin-orbit modulation and charge manipulation by directly controlling the density of states on picosecond timescale. Experiments were performed on p-type Bi₂Se₃, a promising candidate for spin-based devices^{14,15}, and ideal since it exhibits both a strong SPV effect in the bulk^{27,28} and 2D QW Rashba surface states, with the latter readily produced through various surface dopants such as carbon monoxide, water, potassium, rubidium, or even long exposure to vacuum^{11–13,20,29–32}.

RESULTS

Gating surface QWs with light

Figure 1 presents a schematic of the experimental setup and the effect of infrared light pulses on the band-bending and QW state. In a semiconductor, the SPV effect occurs when in-gap surface states lead to a redistribution of charge between the bulk and surface at equilibrium. This non-uniform charge distribution is called the space charge region and produces an internal electric field that 'bends' the bands near the surface, as schematically shown in Fig. 1a. In the case of downward band-bending, illumination of the surface via an infrared pulse generates photoexcited electrons and holes that drift to the surface and bulk, respectively. These carriers partially cancel the internal electric field thereby reducing the band-bending and altering the surface potential (solid yellow region)^{33,34}. Equivalently, the downward band-bending potential results in an internal electric field at equilibrium, (E_{BB}), and this electric field is reduced by an opposing electric field generated by the separated photoexcited charges. The consequence of this is a time-varying electric field in the bulk that decays according to the recombination of separated photoexcited electron holes. Hence, an SPV semiconductor

¹Department of Physics, University of California, Berkeley, CA 94720, USA. ²Materials Science Division, Lawrence Berkeley National Laboratory, Berkeley, CA 94720, USA.

email: sciocys@berkeley.edu; alanzara@lbl.gov

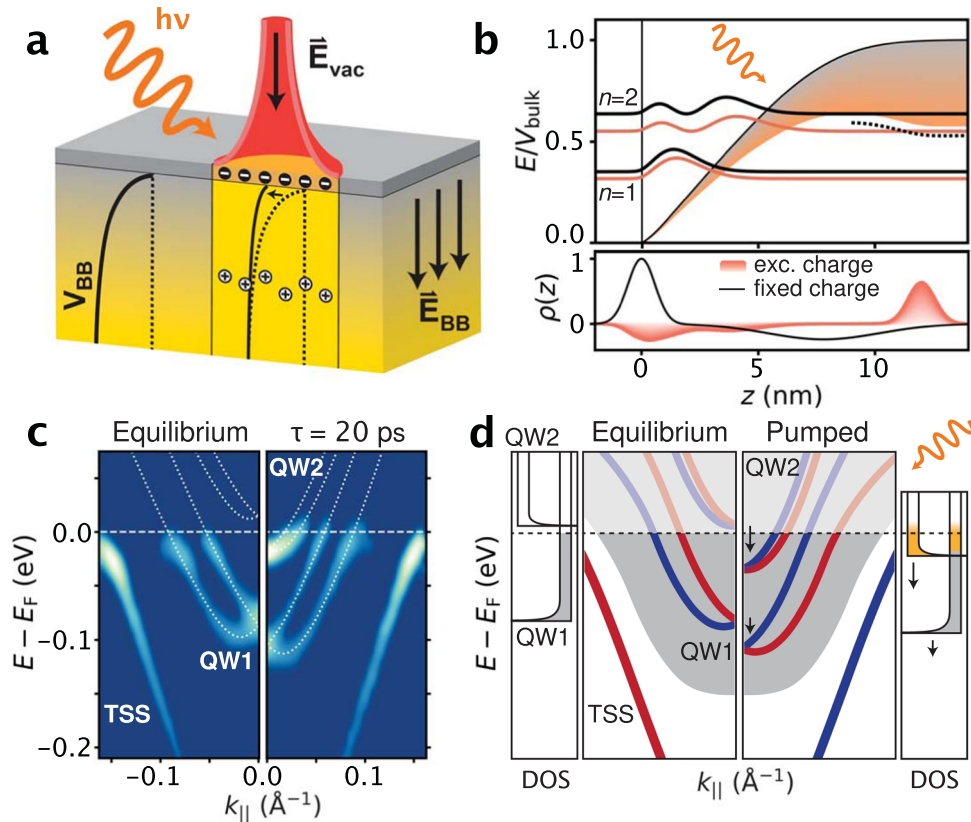


Fig. 1 Tuning quantum well potentials through charge separation. **a** Diagram of the band-bending in Bi_2Se_3 inside and outside the illuminated region. Infrared excitation generates excited electron-hole pairs that are separated by the band-bending, reducing the internal electric field. **b** Photoexcited charge separation decreases the slope of the quantum well potential (gray to orange region). The quantum well energy levels ($n = 1, 2$) before illumination (solid curves) are compressed in energy after the pump (dotted curves). **c** $\partial^2/\partial E^2$ spectra at equilibrium and after pump pulse demonstrating the spectrum modification. **d** Illustration of quantum well level shifts in Bi_2Se_3 before and after illumination. The gray parabolic region represents the conduction band before quantization. The DOS of Rashba-split bands exhibits a singularity near the band bottom. The photo-induced spectrum modification enables toggling of a Lifshitz transition.

substrate can serve as a time-dependent electric gate to 2D electronic states at the surface, and the infrared pulse can be focused to gate a specific area of interest. The Bi_2Se_3 samples have metallic surfaces due to a topological surface state and host QW states which can be modified by the pump-induced time-dependent charge separation. In this way, the surface of the SPV material itself is the subject of the electric field gating and is modified by the time-varying internal field. An added consequence of the photo-induced charge separation is that the resulting finite dipole at the surface also produces an external electric field between the sample and the detector, \mathbf{E}_{vac} , that affects the detected kinetic energy of the photoelectron, resulting in a rigid energy shift of the measured dispersion, allowing us to track the SPV in real-time^{27,35–38}.

The Bi_2Se_3 samples in this study are p-type doped with a hole-like majority carrier concentration of $\approx 1 \times 10^{19} \text{ cm}^{-3}$ (see Supplementary Fig. 3), yielding a fairly conductive bulk that generates a narrow SCR at the surface of $\sim 10 \text{ nm}$ (see discussion). In panel b, we have modeled the effect of an optical pump on the band-bending potential and QW energy levels. The lower plot shows the distribution of fixed charges that form the equilibrium band-bending potential (black line) and separated charges following photoexcitation (red gradient). Photoexcited electrons are distributed equally in three parts between the surface and two QWs (using the QW wavefunctions to determine the density profile) and an equal number of photoexcited holes piled at the edge of the SCR. The band-bending length-scale is similar to the wavefunction spatial extension near the surface, such that only sufficiently separated charges on either side of the SCR can avoid

high recombination rates in order to form a persisting SPV effect³⁹. The amplitudes of the excited charges with respect to the fixed charges have been exaggerated by 2x for visibility. The effect of the population of separated photoexcited charges on the QW potential is seen in the upper plot (gray to orange). A secondary well forms at the bulk edge of the SCR (see dotted curve in panel b) that limits the ability to trap holes in the bulk such that the QW potential is not quenched after SPV saturation at the highest fluence (saturation is shown later in Fig. 5b). The squared modulus of the wavefunctions and corresponding energies have been calculated for the equilibrium and maximally pumped condition shown as black and dark orange curves, demonstrating compression of the energy eigenvalues.

Figure 1c presents $\partial^2/\partial E^2$ ARPES spectra demonstrating the compression of the QWs after pump excitation as also schematically summarized in Fig. 1d. The strong downward band bending at equilibrium leaves the surface n-type doped, filling a large portion of the upper Dirac cone, and the quantized conduction band^{10,12,27}, despite the p-doping in the bulk. The first and second QWs, QW1, and QW2 are derived from the bulk conduction band (gray parabolic region in panel d) and exhibit near-parabolic dispersions. The strong spin-orbit coupling inherent to Bi_2Se_3 as well as inversion symmetry breaking at the cleave-plane generates a Rashba effect that duplicates the QW states into momentum-separated spin-polarized pairs (shown in red and blue in panel d)^{8–10}. Furthermore, the momentum splitting transforms the band minimum from point-like to a one-dimensional ring, resulting in a van Hove singularity below the intersection of the Rashba bands⁴⁰ for both QW1 and QW2 (see DOS in panel d). At equilibrium, with

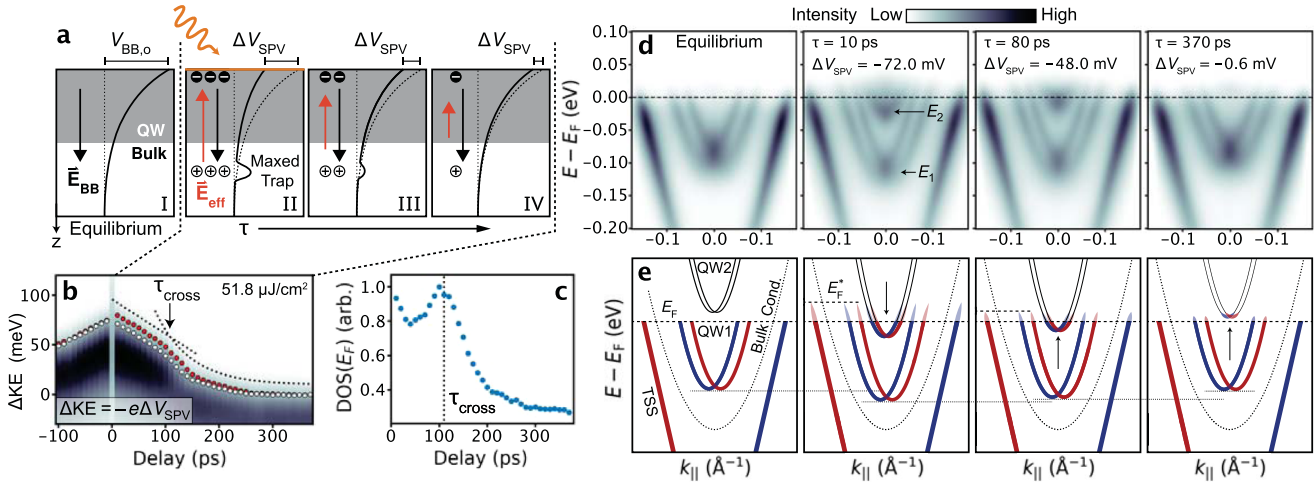


Fig. 2 Time-resolved electric field gating of quantum well spectrum. **a** Effective applied field, \mathbf{E}_{eff} is generated by separated photoexcited carriers, manifesting as a reduction of the band-bending potential. SPV is maximized before quenching the band-bending due to a finite limit on trapped holes. As photoexcited charge recombines, band-bending returns, and the effective field is reduced. **b** Separated surface charge can be monitored by the rigid energy shift of the ARPES spectrum due to the voltage change at the surface (ΔV_{SPV}). Black-lined white dots correspond to the SPV-induced rigid shift of the band structure relative to equilibrium E_F , red dots correspond to the quasi-Fermi level at k_F of the TSS. **c** DOS at the Fermi level as a function of delay revealing the Lifshitz transition of QW2. **d** Symmetrized ARPES spectra at equilibrium and three non-equilibrium delays demonstrating the pump-induced quantum well shifts after correcting the SPV shift. **e** Graphic summarizing quantum well spectrum dynamics corresponding to the spectra in **d**, presenting a delay-dependent field effect on the quantum wells and long-lived quasi- E_F .

no pump beam, only QW1 is populated, exhibiting strong Rashba splitting. After pumping with a $51.8 \mu\text{J cm}^{-2}$ 820 nm pulse, QW1 and QW2 shift downwards in energy relative to the bulk conduction band minimum. QW1 shifts downward by ~ 25 meV and QW2 emerges below E_F and is subsequently populated resulting in a sudden increase of the DOS. Therefore, the light-driven modification and subsequent filling of QW2 drives a van Hove singularity below the Fermi level, inducing a Lifshitz transition⁴¹.

Dynamic QW spectrum and Lifshitz transition

Figure 2 demonstrates the evolution of the QW spectrum after ultrafast illumination. Since the SPV decays in time and the effective gating field depends on the SPV strength, a single time-resolved measurement records a continuum of the field effect on the QW.

Figure 2a illustrates the field effect on surface-confined QW as a function of delay. The gray region denotes the QW SCR confinement at the surface and the white region represents the near-surface bulk. At equilibrium (I), the band-bending is maximally resulting in an enhanced slope for the QW potential and can be represented by an internal electric field \mathbf{E}_{BB} . The maximum reduction in the band-bending is the potential difference between the surface and deep within the bulk at equilibrium, labeled $V_{\text{BB},0}$. At $\tau = 0$ (II), when the pump pulse arrives, separated photoexcited carriers generate an opposing electric field to \mathbf{E}_{BB} , labeled \mathbf{E}_{eff} . The internal field from the separated carriers acts as an effective applied field on the QW potential, driving the time-dependent modification to the spectrum. In the illustrated scenario, the pump pulse is significantly strong as to saturate the available hole trap sites altering the surface potential as a function of delay by $\Delta V_{\text{SPV}}(\tau) = V_{\text{BB},0} - V_{\text{BB}}(\tau)$, resulting in reduced but non-zero band-bending. At more positive delays (III–IV), the excited charge recombines thus reducing the effective field \mathbf{E}_{eff} , reviving the band-bending potential, and bringing the surface potential back to its equilibrium value.

We can monitor the photoexcited charge separation through the energy shift of the ARPES spectrum induced by the in vacuum

field produced by ΔV_{SPV} . The change in the surface potential has the effect of increasing the photoelectron kinetic energy at the detector with respect to the equilibrium energy position (ΔKE). Figure 2b presents the effect of the SPV rigid shift on the topological surface state at the Fermi wavevector as a function of delay. The rigid shift of the spectrum extracted from the shift of the Dirac dispersion at fixed momenta well below E_F is plotted in white. The Fermi edge as determined by fitting a Lorentzian multiplied by a Fermi-Dirac distribution is plotted in red and denotes the quasi-Fermi level, E_F^* (See Supplementary Fig. 2). The rigid energy shift is a direct measure of the surface potential as a function of delay since $\Delta\text{KE}(\tau) = -e\Delta V_{\text{SPV}}(\tau)$, where e is the charge of the electron.

Under the center of charge approach^{42,43}, the SPV signal can be described by an average displacement of electron and hole sheet charges induced by the band bending such that:

$$\Delta V_{\text{SPV}} = \frac{e}{\epsilon_r \epsilon_0} n_{\text{sep}} d, \quad (1)$$

where n_{sep} and d are the charge separation density and separation distance, respectively, and $\epsilon_r \epsilon_0$ is the dielectric constant of Bi_2Se_3 . With the assumption that the separation distance is fixed and approximately equal to the width of the band-bending region, then the measurement of ΔV_{SPV} is proportional to the charge separation concentration n_{sep} , and therefore the charge at the surface^{42,44}. To be clear, this is different than the total photoexcited carriers generated by the pump since significant recombination has taken place after 10 ps, with only sufficiently separated charges surviving (see Supplementary Fig. 5).

Moreover, if the charge is sufficiently separated and localized (a fit assumption based on the long lifetime of the SPV), then the photo-induced charge separation is analogous to a parallel plate capacitor within the probe beam spot and the effective applied field is also proportional to ΔV_{SPV} and the surface charge. Therefore, the ΔKE shift (panel b for $\tau > 0$) decays proportionally to the separated charge density (panel b for $\tau > 0$), enabling us to map the delay axis to a surface voltage and ultimately an applied field strength (discussed in Fig. 3).

At negative delays (photoemission occurs before the pump) there is a rigid shift of the recorded ARPES spectrum. This effect is

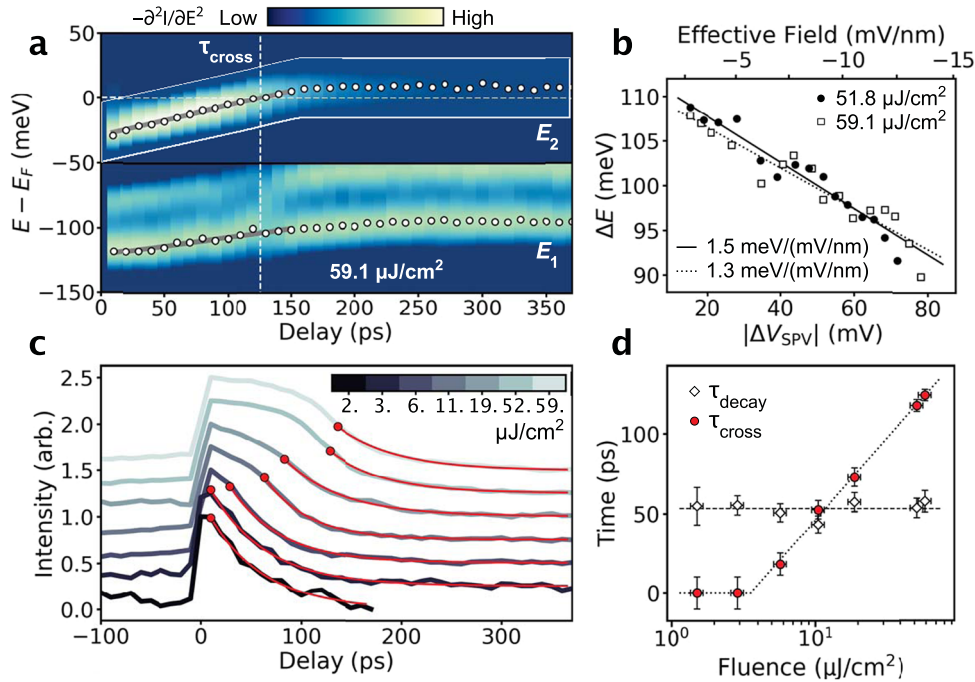


Fig. 3 Quasi-equilibrium charge and ultrafast intersubband-gap control. **a** $\partial^2/\partial E^2$ spectra of QW1 and QW2 band bottoms as a function of delay. The band bottom positions are marked by black-lined white dots demonstrating a near-linear recovery up to the moment E_2 crosses E_F , τ_{cross} . **b** The intersubband-gap as a function of the SPV determined at each delay for the two highest fluences (51.8 and $59.1 \mu\text{J}/\text{cm}^2$). The effective field on the quantum well system is extrapolated from the average best fit line and the triangular-well approximation. **c** Integrated spectral intensity of the QW2 band bottom using integration window in **a** over a large fluence range. E_F crossing time, (τ_{cross}), +10 ps is used as a cutoff (minimum set at 10 ps) for exponential fits (red). **d** QW2 decay rate, τ_{decay} , (black open diamonds) and τ_{cross} (red dots) as a function of maximum SPV at each fluence (and extrapolated effective field on QWs) indicating that the lifetime of QW2 states above E_F is fixed but quasi-equilibrium lifetime is set by peak field strength. **d** y axis error bars are from fit covariance in **c** (τ_{decay}) and linear fit in Supplementary Fig. 9 (τ_{cross}), fluence error is 10% conservatively.

due to the photoelectron interacting with an SPV-generated field induced by a pump pulse that arrives after photoemission^{35–38}. The rigid energy shift in the negative delay is therefore shifting the unpumped spectrum and can be ignored for the purposes of this study.

In the positive delay, a maximum ΔKE shift of 72.0 meV is reached at 10 ps after $51.8 \mu\text{J}/\text{cm}^2$ illumination. Between 10 ps and 125 ps, the SPV-induced shift follows an unusual linear decay profile. After 125 ps the SPV decays exponentially with a time constant of ~ 53 ps. This apparent discrete transition from a linear decay mechanism to an exponential decay is associated with the transit of QW2 above the Fermi level, τ_{cross} . In the absence of surface QWs, Bi_2Se_3 exhibits a simple exponential decay with no linear region or kink^{27,38}. Panel c shows the DOS at the Fermi level, $E = (-0.005, 0.005) \text{ eV}$, and at zero momentum, $k = (-0.005, 0.005) \text{ \AA}^{-1}$, demonstrating the crossing of the QW2 band bottom and indicating the Lifshitz transition as QW2 relaxes.

The continuous photo-induced modification of the QWs is observed in Fig. 2d which displays four spectra of the Bi_2Se_3 QW spectrum at equilibrium and at three separate delay values and then schematically simplified in Fig. 2e. The spectra have been shifted to compensate for the extrinsic delay-dependent rigid energy shift associated with the SPV effect (black-lined white dots in panel b)^{35–38}. At equilibrium (far left), only the topological surface state and QW1 are present and occupied below the Fermi level, E_F . The full band-bending is present creating a steep QW potential as we described in scenario I of panel a. This results in a large energy spacing for QW1 and QW2, leaving QW2 unpopulated above E_F .

For the pumped spectrum, we first look at the data at 10 ps. By this time, nearly all hot carrier recombination has already taken place^{45–47}, leaving behind long-lived trapped charges (see

Supplementary Fig. 4). QW1 shifts downward in energy and QW2 falls below E_F as photoexcited charges have reduced the equilibrium band-bending modifying the QW potential; QW2 is subsequently filled below E_F and states above E_F are populated resulting in a new quasi-equilibrium Fermi level. At $\tau = 80$ ps, the QW spectrum drifts towards higher energies relative to the topological surface state and E_F . The competition between the rate of charge being pushed above E_F by the upward energy shifts (dotted horizontal lines in Fig. 2e) and the decay rate of charge above E_F allows charge to exist above the Fermi level during the course of the spectrum relaxation. This ultimately leads to excess charge remaining in QW2 at $\tau = 370$ ps even when the QW energy spacing has returned to equilibrium. For each delay, we can determine the photo-induced change in the surface potential, $\Delta V_{\text{SPV}}(\tau)$, from ΔKE in panel b, thereby tracking the QW modifications as a function of surface voltage.

Reduction of QW spacing and prolonged charge storage

We further investigate the delay dependence of the QW level spacing and charge occupation in order to better understand the pump-induced QW state modification. In Fig. 2, we demonstrated that the surface potential is a function of delay, and so we are able to track the QW modification with respect to surface voltage. We can take this one step further and estimate the effective field, E_{eff} , from the energy positions of the QW1 and QW2 band bottoms.

Figure 3a displays momentum integrated $\partial^2/\partial E^2$ spectra for QW1 and QW2 band bottoms as a function of delay. The momentum integration windows for QW1 and QW2 band bottoms are centered at $k = 0.000 \text{ \AA}^{-1}$ and $k = 0.023 \text{ \AA}^{-1}$, respectively, with a width of $\Delta k = 0.002 \text{ \AA}^{-1}$. The QW1 and QW2 band bottom positions, E_1 and E_2 , (black-lined white dots) track the evolution of the energy levels as the QW spectrum is modified

by the field effect and subsequent relaxation. The positions of E_1 and E_2 are displayed in Fig. 2d for comparison with the full dispersion. After pump illumination, QW1 and QW2 shift toward higher binding energies, dropping QW1 by ~25 meV and QW2 by ~35 meV and bringing QW2 ~25 meV below E_F . Both QWs shift back towards lower binding energies linearly as a function of delay at different rates. For QW2, 126 ps corresponds to τ_{cross} (see vertical dashed line in panel a), the delay time in which the band bottom crosses E_F . After this point, the spectral intensity of the band bottom decreases at an accelerated rate.

An important property of QW systems is the intersubband-gap, defined as the difference in energy between the QW2 and QW1 band bottom energies $\Delta E = E_2 - E_1$, which sets crucial material properties including the optical response. The delay dependence of the QW band bottom positions, and therefore the surface potential dependence of the intersubband-gap, demonstrates ultrafast-field tunability. Panel b shows the potential dependence of the intersubband-gap ΔE for the two highest fluences. We focus on the band-gap values for $\tau < \tau_{\text{cross}}$ where QW2 is fully populated and the position of the band bottom is not strongly influenced by the Fermi level.

The effective applied field on the QW spectrum can be extrapolated from the intersubband gap. The triangular-well potential is a widely used approximation to describe surface confinement, especially for low-energy wavefunctions, and is suited for capturing the effective electric field experienced by the QWs (see Supplementary Fig. 7d). A more precise model of the confinement potential may be necessary for the condition of higher-energy wavefunctions ($n > 2$)^{12,48–50}.

The triangular-well potential is described by, $V(z) = eFz$, in which F represents the steepness of the well with units of the electric field. As such, the QW wavefunctions take on the form of Airy functions with energy eigenvalues^{48,50}:

$$\epsilon_n = c_n \left[\frac{(eF\hbar)^2}{2m^*} \right]^{1/3}, \quad (2)$$

The energy eigenvalues, ϵ_n , are referenced to the bulk conduction band minimum before quantization, which represents the bottom of the QW potential. By subtracting ϵ_1 from ϵ_2 , the equation can be rearranged to solve for F using only the intersubband-gap energy, and the known Airy coefficients, $c_2 \approx 2.338$ and $c_1 \approx 4.088$.

$$F = \frac{\sqrt{2m^*}}{e\hbar} \left(\frac{\Delta E}{c_2 - c_1} \right)^{3/2} \quad (3)$$

Utilizing the above equation and the average best fit lines from panel b, the x axis can be rescaled in terms of the effect applied field on the QW states. We use the average effective mass from dispersion fits of $m^* = 0.45 m_e$. The total electric field in the QW region at equilibrium ($\Delta V_{\text{SPV}} = 0$) is 42.0 mV nm⁻¹ and 55.7 mV nm⁻¹ at the maximal SPV ($\Delta V_{\text{SPV}} = 78.5$), reasonable electric field values for surface QW systems²³. This is equivalent to applying a field, \mathbf{E}_{eff} between 0 mV nm⁻¹ ($\Delta V_{\text{SPV}} = 0$ mV) and 13.7 mV nm⁻¹ ($\Delta V_{\text{SPV}} = 78.5$ mV) opposite to the equilibrium band-bending field \mathbf{E}_{BB} .

The field effect on the intersubband-gap shown in Fig. 3b exhibits a nearly linear dependence since the QW electric field, F , is always far from 0, existing in the range of (40–60 mV nm⁻¹). The applied field axis ticks are determined by the y axis values of the best fit line and are independent of the surface voltage axis. The even spacing of both x axis ticks demonstrates that the intersubband gap is near-linear in both surface voltage and effective electric field, as expected from the center of charge separation model in Equation (2).

In addition to enabling an ultrafast-field effect on the QW energy positions and intersubband-gap, the ultrafast gating grants

access to the charge dynamics of the QW spectrum. In particular, we uncover quasi-equilibrium charge occupation and determine recombination timescales, not accessible by any static gating technique. Furthermore, we observe that the crossing of the QW2 band bottom above E_F (vertical dashed line in Fig. 3a, $\tau_{\text{cross}} = 126$ ps at $59.1 \mu\text{J cm}^{-2}$) corresponds to the transition of the SPV relaxation from a linear to an exponential decay mechanism as observed in Fig. 2b. Figure 3c displays the integrated spectral intensity of the QW2 band bottom as a function of delay (shaded region in panel a) for fluences between 1.5 and $59.1 \mu\text{J cm}^{-2}$, showing stable charge storage before fluence-dependent τ_{cross} values that then depopulate exponentially. At the lowest fluences, there is no stable region and only exponential behavior. The decay region in red is fitted with exponential fits, with the start of the fitting range (red dots) set by $\tau_{\text{cross}} + 10$ ps and a minimum cutoff of 10 ps.

As a function of fluence, the resulting timescales from the exponential fit, τ_{decay} , are plotted in Fig. 3d (diamonds) alongside τ_{cross} (red dots). The decay rate of charge in QW2, τ_{decay} , is independent of fluence with an average decay time of 53 ps. On the other hand, τ_{cross} increases logarithmically for fluences above $4 \mu\text{J cm}^{-2}$, marking a critical fluence for the Lifshitz transition of QW2. For fluences in which the $\tau_{\text{decay}} = 0$, QW2 never dips below E_F after the pump, and therefore does not undergo a Lifshitz transition. All together, this demonstrates that the charge stored in QW2 is stable while it is below E_F and charge above E_F decays with a timescale of ~53 ps. Moreover, the timescale for stable stored charge in QW2, τ_{cross} , is a consequence of the dynamic Lifshitz transition and can be controlled by varying the pump fluence, equivalent to increasing the SPV strength.

Ultrafast reversible reduction of Rashba splitting in QW1

Another appealing capability of time-resolved photo-gating is the ultrafast control and tunability of the Rashba splitting since the Rashba effect depends on the inversion symmetry breaking electric field at the surface and can therefore be tuned by an applied field^{51–53}. The Rashba effect is an energy splitting that is, in the simplest form, linear in momentum with $\Delta E_R = \alpha_R k$ where $\alpha_R k$ is known as the Rashba parameter. In the case of parabolic bands, this leads to a rigid splitting in momentum $k_0 = \alpha_R m / \hbar$ ^{229,54}. By directly fitting the bands, we can obtain an accurate determination of α_R . In Fig. 4a, we present the band fitting of the Rashba-split QW1 band at equilibrium and $\tau = 30$ ps after the pump. The momentum positions of the Rashba bands as a function of energy (red and blue dots) were determined by peak fitting the momentum distribution curves along delay-dependent binding energy ranges and avoiding the Rashba crossing at Γ .

In panel b, the delay dependence of the Rashba splitting is clearly seen in the QW1 band bottom momentum positions captured by integrating the second derivative in energy spectra from panel a over a narrow energy range 15 meV below the dispersion, avoiding the increased intensity at the Rashba intersection at Γ . The black dashed curve serves as a guide to the eye, indicating a 15% reduction in k_0 at $\tau = 0$ that returns to equilibrium. The peak positions for the negative-momentum band bottom are plotted in pink and closely follow the 15% reduction.

Figure 4c presents the resulting change in Rashba parameter (yellow dots) as a function of delay at high pump fluence ($59.1 \mu\text{J cm}^{-2}$) as determined by the dispersion fits in panel a. In the negative delay, the Rashba parameter remains constant at its equilibrium value. Upon illumination the Rashba parameter drops by ~15% and then linearly returns towards equilibrium up until ~125 ps (vertical arrow). From then on, the Rashba parameter exponentially returns to the equilibrium value on a timescale of 53 ps. The decay behavior of the Rashba parameter closely matches the SPV decay (black open dots) in which linear decay transitions into an exponential decay near 125 ps. This

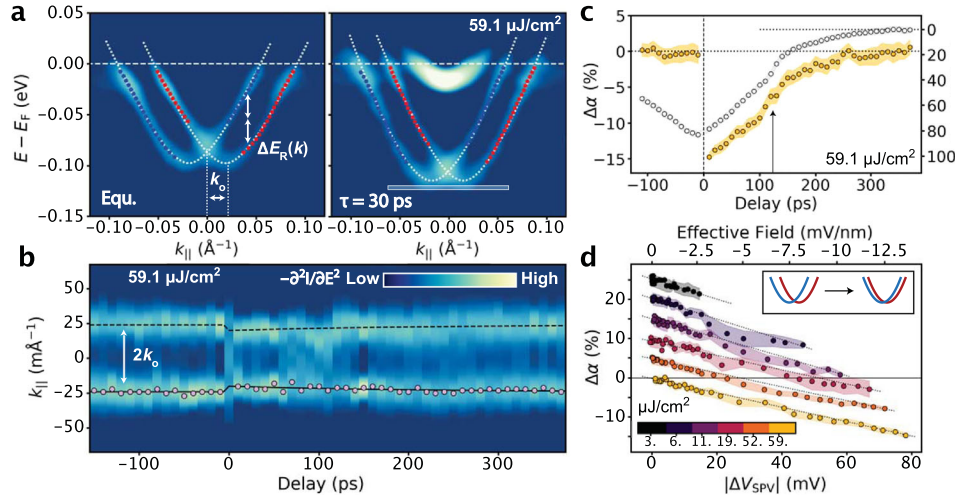


Fig. 4 Ultrafast-field effect on Rashba splitting. **a** $\partial^2/\partial E^2$ non-symmetrized spectra of quantum well states at equilibrium and 30 ps. Red and blue dots correspond to respective spin-split Rashba band positions for QW1. **b** $\partial^2/\partial E^2$ non-symmetrized spectra integrated 15 meV below QW1 band bottom as a function of delay. Pink dots indicate peak positions on the negative- k band bottom, black lines represent 15% reduction in k_0 after pump that relax to equilibrium. **c** Percent change of the Rashba parameter (yellow) as a function of delay compared to the delay-dependent SPV (black open dots) at $59.1 \mu\text{J cm}^{-2}$. After pump excitation, Rashba parameter drops by 15% and experiences a linear onset to exponential recovery (vertical arrow). **d** Percent change of the Rashba parameter versus SPV (and extrapolated effective field) over a large fluence range. Each fluence measurement is spaced by 5% for visibility. Shaded outlines in **c** and **d** represent error propagated from covariance in fits from **a**.

demonstrates a linear relationship of the Rashba effect with respect to the surface photovoltage and therefore the applied effective field, and subsequently dependent on the dynamic Lifshitz transition.

Figure 4d plots the percent change of the Rashba parameter as function of the SPV at each delay as well as the extrapolated effective field on the QW. The curves are spaced artificially by 5% intervals for clarity. The field effect behavior of the Rashba parameter is linear for all fluences, decreasing as the applied field is driven to more negative values with $\sim 15\%$ reduction in Rashba splitting at a maximal applied field of 13.5 mV nm^{-1} . From the average of the fluence measurements, the response of the Rashba parameter versus field strength is $1.26 \pm 0.21\% \text{ nm mV}^{-1}$. This ultimately demonstrates precise control of the Rashba splitting of the QW states with ultrafast photo-gating, with the Rashba parameter tuned by the pump pulse intensity and dependent on the Lifshitz mediated relaxation.

Lifshitz-dependent surface charge trapping

Finally, in Fig. 5 we report a non-monotonic dependence of the quasi-Fermi level, E_F^* , with respect to fluence that demonstrates the significance of the Lifshitz transition on the infrared response of the QW system.

The delay dependence of E_F^* for all measured fluences is plotted in Fig. 5a. E_F^* is measured in reference to the equilibrium Fermi level (i.e. the difference between the red fit and white fit from Fig. 2b). For fluences above $4 \mu\text{J cm}^{-2}$, E_F^* is offset from equilibrium starting in a plateau region for delays less than τ_{cross} preceding a small peak after τ_{cross} that leads into exponential decay. Curiously, the offset at early delays is non-monotonic with fluence, peaking at $\sim 15 \text{ meV}$ for $5.7 \mu\text{J cm}^{-2}$ and leveling off towards $\sim 5 \text{ meV}$ at high fluence. The encircled points indicate the values that are averaged to generate the E_F^* offset values in panel e. The hump that occurs near τ_{cross} , may be indicative of a large charge transfer from QW2 to the TSS following the reverse Lifshitz transition of the QW2 singularity. This may additionally suggest that the sustained E_F^* plateau region is also from the charge in the QW states leaking into the TSS during relaxation. For the purposes of this study, we focus on E_F^* at early delays. The relatively small offset of E_F^* is in contrast to previous time-resolved studies on p-type Bi_2Se_3 -

related samples without QWs²⁴, emphasizing the influence of QW1 and QW2 on the relaxation dynamics.

The behavior of E_F^* at early delays with respect to pump fluence can be explained within the framework of the stored equilibrium charge in QW1 and QW2 described in Fig. 3. To start, in Fig. 5b we display the fluence dependence of the maximal SPV, $|\Delta V_{\text{SPV}}(\tau = 10 \text{ ps})|$, which is proportional to the initial net charge at the surface after hot carrier relaxation, $\Delta n_{\text{surf}} = n_{\text{sep}}$. Next, the fraction of charge stored below E_F in QW1 and QW2 is calculated. To do this, we use linear extrapolations of the QW1 and QW2 band bottom positions as a function of SPV from the high fluence data in Fig. 3a and the cumulative DOS of Rashba-split parabolic bands shown as dashed blue curves (see Supplementary Fig. 8f). The band bottom positions, and therefore the cumulative DOS, are functions of the SPV strength and are calculated from the phenomenological fit of the SPV maximal values (dashed red curve). The sum of the QW1 and QW2 cumulative DOS corresponds to the total available quasi-equilibrium charge states for photoexcited charge (solid blue curve).

Figure 5c depicts two photoexcitation regimes that summarize the role of the Lifshitz transition on E_F^* . The brackets on the left indicate the pump-induced QW energy shift from equilibrium positions, the blue and red regions correspond to excited charge below and above E_F , respectively. At moderate fluences of $3\text{--}7 \mu\text{J cm}^{-2}$ QW2 undergoes a Lifshitz transition, however, only QW1 has significant available states below E_F leaving excess separated charge to populate above E_F . At high fluence, QW2 has shifted well below E_F enabling a large degree of quasi-equilibrium charge storage reducing the burden on states above E_F .

To further quantify the effect, it is more useful to reparameterize the curves of panel b in terms of the surface voltage to avoid reliance on the SPV phenomenological fit. In this way, the total net charge concentration is a linear function and the QW1 and QW2 band bottoms are linearly dependent on the x axis. Because the QW1 and QW2 band bottom positions are empirically determined, the only consequential free parameter is the relative amplitude of the total available quasi-equilibrium charge states (blue regions) with respect to n_{surf} (dashed black line). The difference between the aforementioned populations represents the excess photo-excited charge at the surface (light-red region), which describes

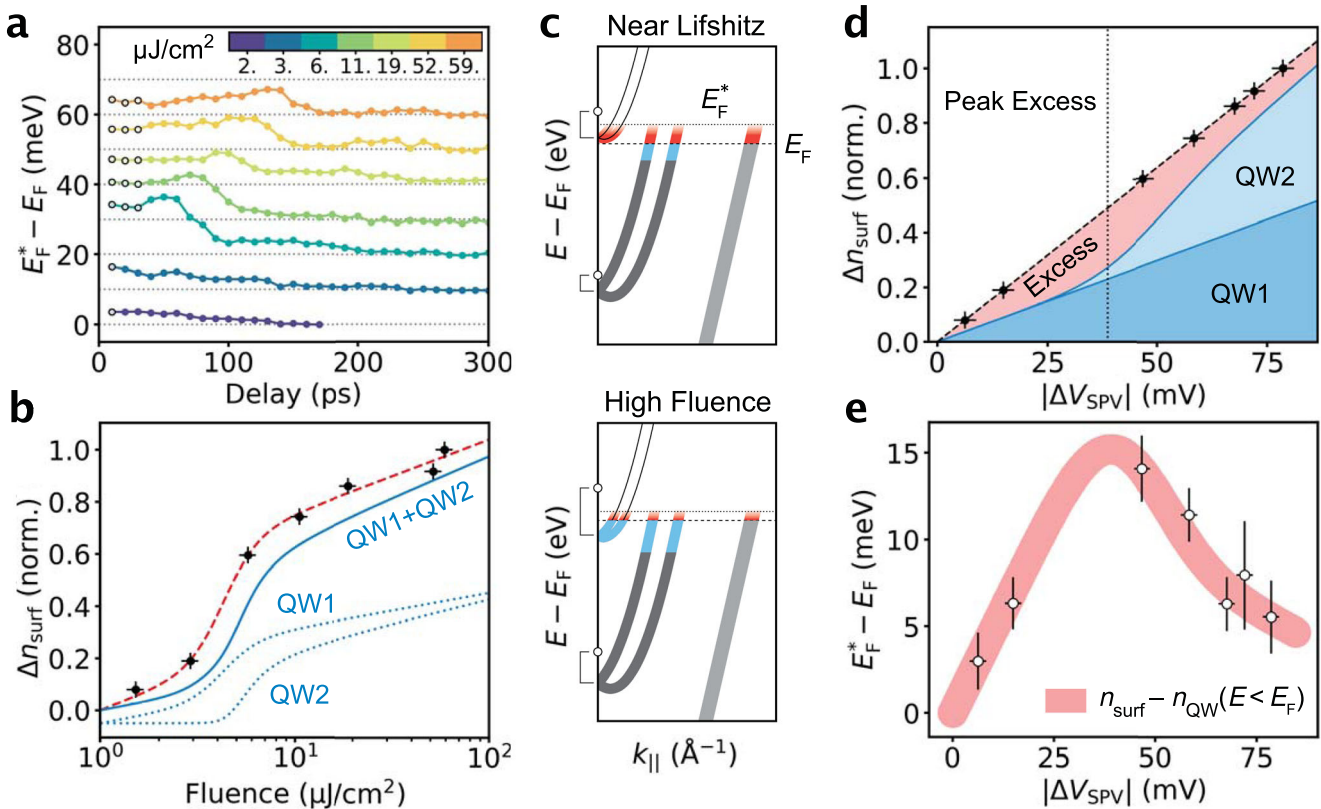


Fig. 5 Competition between surface state trapping and quasi-Fermi level. **a** Quasi-Fermi level as a function of delay for all fluences. Outlined points indicate averaged points used in **e**. **b** Maximal SPV as a function of fluence indicating separated charge concentration at the surface. Labeled blue curves demonstrate QW1 and QW2 states below E_F determined from the phenomenological fit (dashed red) and the SPV dependence of the band bottom positions in Fig. 3a. **c** Graphical comparison of quasi-Fermi level shift between medium and high fluence. Medium fluence ($3\text{--}7\ \mu\text{J cm}^{-2}$), QW2 photo-carrier generation is significantly larger than available states in shifted QWs. At high fluence, photo-carrier generation has saturated and QW2 provides increased storage below E_F . **d** Representation of **b** with the x axis parameterized by SPV surface potential. Excess carriers after filling QW trap states (light-red) contribute to raising E_F^* (black-lined white dots). **e** E_F^* at short delays from **a** and total surface charge minus trapped surface charge (light-red curve)(black dashed curve minus solid blue curve in **d**) as a function of surface voltage. Error bars for Δn and ΔV_{SPV} are conservative 10% and 2.5 meV, respectively. Y axis error in **e** determined by difference between E_F^* measured at QW1 and TSS k_F .

the charge remaining after QW1 and QW2 are filled below E_F and that must occupy above- E_F states. From panel d, it is clear that the emergence of the QW2 band bottom below E_F , which acts to enhance the DOS contribution of QW2 below E_F , necessitates a peaked behavior in the excess charge population near the Lifshitz transition, regardless of the fluence dependence of the SPV effect.

The proportionality factor between the charge stored in QW1 and QW2 with respect to n_{surf} is chosen such that the excess charge best fits the E_F^* offset plotted in panel e. The excess charge from the model in panel d closely captures the non-monotonic behavior in the measured E_F^* values.

DISCUSSION

Using the reported dielectric constant of Bi_2Se_3 of a nominal $\epsilon_r \approx 30\text{--}100$ ^{55,56}, we can extract an approximate SCR width, describing the spatial extent of the band-bending utilized in Fig. 1b, $d = \sqrt{2\Delta V_{\text{BB},0}\epsilon_r\epsilon_0/en_A} \approx 10\ \text{nm}$ ³⁴, where the acceptor ion concentration, n_A , is approximately equal to the bulk majority carrier density in the SCR and $V_{\text{BB},0} \sim 300\ \text{mV}$ based on the observation of the QW3 energy level at short delay and the zero-point energy of the QW spectrum (see Supplementary Fig. 6). A second independent method is to use charge conservation at the SPV saturation, since band-bending cancellation occurs when the total surface charge is equal to the volumetric bulk charge times the depth. The maximal surface charge can be calculated by

Luttinger's theorem⁵⁷ on the QW1, QW2, and TSS bands giving $5 \times 10^{12}\ \text{cm}^{-2}$ (see Supplementary Fig. 8), and since only $\sim 1/4$ (from $\Delta V_{\text{SPV}}/V_{\text{BB},0}$) of the charge is screened in the SCR we get, $d = 5 \times 10^{12}\ \text{cm}^{-2}/(1 \times 10^{19}\ \text{cm}^{-3}/4) \sim 10\ \text{nm}$. These estimates ignore possible variations in both the dopant concentration and dielectric constant between surface and bulk, as well as hexagonal deformation and possible non-isotropic charge storage at the Fermi surface^{20,58}. However, the approximate SCR width is consistent with the band-bending length-scale observed previously in Bi_2Se_3 ⁵⁹.

Initial reports of the Rashba effect on metallic surfaces suggested that applied fields on the order of $1000\ \text{mV nm}^{-1}$ are insufficient to produce the observed Rashba effect, and that the nuclear core potentials are responsible for large splittings^{52,60}. In our experiment we observe a 15% reduction on an $\sim 1\ \text{eV \AA}$ Rashba effect with fields near $10\ \text{mV nm}^{-1}$ only. There is a large body of evidence demonstrating small changes to surface or interface fields generate large changes to the Rashba parameter^{51,61,62}. A reasonable explanation that has been presented is that the applied field plays an indirect role on the Rashba effect by shifting electrons to and from the nuclear cores at the surface plane^{53,61,63–65}. With respect to Bi_2Se_3 , Ereemeev et al. presents a debated hypothesis on the origin of the QWs from surface modulated van der Waal's gaps⁶⁶. Although the origin of the QWs has been further argued to be from surface band-bending^{20,30}, their study indirectly demonstrates the role of wavefunction

overlap with the surface-most quintuple layer as a key ingredient to the Rashba effect. We have shown through our simplified band-bending calculation of the QW wavefunctions in Supplementary Fig. 7e that the shift in QW position is field-linear and nearly 2 Å over 10 mV nm^{-1} , a significant fraction of the quintuple layer thickness. In totality, our results are consistent with a picture that the origin of the Rashba splitting is largely controlled by wavefunction overlap with asymmetric nuclear potentials within the first quintuple layer, controlled linearly by the field.

One consequence of the ultrafast QW modification is a large rapid and reversible change in the DOS at the Fermi level. This is made possible by the emergence of QW2 below E_F after pump excitation; changing the topology of the Fermi surface and triggering a reversible Lifshitz transition. The kink in the relaxation of the SPV as well as the Rashba modification is correlated with τ_{cross} , indicating that the reversal of the Lifshitz transition plays a key role in the relaxation. Furthermore, the new states near the Fermi level imply an increase in conductivity at the surface affecting spin-dependent transport properties, and occupation of the QW2 band bottom would influence intersubband optical absorption⁶⁷. As such, this ultrafast-field effect device provides many opportunities for applications that are sensitive to the DOS at the chemical potential and requires further attention exploring the DOS-dependent scattering dynamics.

The SPV photo-gating method can be extended to other semiconductor systems with 2D electron gases. In fact, a similar gating method to the one presented here has been utilized successfully in black phosphorous to drive gap renormalization at the surface^{68,69}. An example of a future application is a heterojunction system in which an exfoliated or MBE-grown 2D material is placed on top of an SPV substrate separated by a thin insulating layer. In this case, a pump pulse focused on the grounded top layer would result in transient gating of the illuminated surface region. Moreover, SPV time constants can vary significantly from picoseconds to milliseconds depending on the system allowing for a large dynamic range of study^{36,69,70}.

In conclusion, we have exposed complex QW dynamics using a time-resolved SPV-based gate. The phenomenology of the photo-induced QW modification is general for surface QW systems because it relies on the surface band-bending of not only topological insulators but many semiconducting systems³⁴. For this system, the unique decay profile of both the SPV and Rashba reduction is contingent on the dynamic DOS near the Fermi level and the existence of a van Hove singularity in the Rashba-split QWs. Accordingly, we have demonstrated local control of the near- E_F DOS; a useful tool for driving electronic phases such as superconductivity⁷¹, magnetism⁷², and, more broadly, correlated phases⁷³. Furthermore, the ultrafast gating mechanism also revealed dynamically stored charge in QW1 and QW2 that ultimately controls the resulting quasi-Fermi level, impossible to observe using static gating techniques. Lastly, we have demonstrated ultrafast reversible modulation of the Rashba effect on 10–100 picosecond timescales opening up the possibility for GHz spin-current manipulation. The temporary photo-induced Rashba tuning creates a platform for spin-orbit modulation enabling light-driven spintronic devices such as ultrafast spin-transistors and photo-controlled Rashba circuitry^{14,74,75}.

METHODS

Sample synthesis and preparation

The p-type Bi_2Se_3 single crystals were grown via directional slow solidification with ≈ 1 at.% Mg substitution with bismuth in order to bring E_F close to the bulk valence band maximum. The crystals were coated in graphite spray and then cleaved in a vacuum along the (111) plane at a base pressure of 5×10^{-11} Torr. The sample experienced rapid dosing triggered by initial exposure to the infrared pump resulting in the formation of a clear QW spectrum similar to the observations by Lin et al.⁸,

with no further dosing occurring after subsequent pumping. This dosing is perhaps due to the presence of trapped gasses in the graphite spray or the crystal itself, and produced results similar to the effects of carbon monoxide and water surface dosing^{12,13}. We have observed this dosing effect multiple times but only after using graphite spray on specifically p-type Bi_2Se_3 samples.

Measurement details

For the pump-probe measurement, we used a pump of 1.48 eV p-polarized photons generated by a cavity-dumped Ti:sapphire oscillator operating with repetition rates of 1357.50 kHz ($51.8 \mu\text{J cm}^{-2}$) and 678.75 kHz (all other fluences). The probe beam consists of 5.94 eV p-polarized photons generated by frequency quadrupling of the 1.48 eV source in two BBO stages⁷⁶. The total time resolution from the two beams is ~ 300 fs. The pump and probe beam spot full-width-half-maxima was 120 μm and 30 μm , respectively. The delay between the pump and the probe is achieved with a mechanical translation stage. Due to the long delay range, careful consideration was taken to ensure that the maximum pointing drift due to the delay stage was minimized to $< 15 \mu\text{m}$. A variable neutral density filter applied to the pump beam enabled fluence-dependent measurements. All reported fluence values indicate incident fluence on the Bi_2Se_3 surface. All spectra were taken at the system's base temperature with liquid nitrogen of ~ 80 K. Data were analyzed using PyARPES analysis framework⁷⁷.

DATA AVAILABILITY

All data and code used for analysis are made available upon request to the corresponding author.

Received: 22 November 2021; Accepted: 14 July 2022;
Published online: 15 August 2022

REFERENCES

- Welsler, R. E. et al. Design and demonstration of high-efficiency quantum well solar cells employing thin strained superlattices. *Sci. Rep.* **9**, 13955 (2019).
- Dupuis, R. D., Dapkus, P. D., Holonyak, N., Rezek, E. A. & Chin, R. Room-temperature laser operation of quantum-well $\text{Ga}_{1-x}\text{Al}_x\text{As-GaAs}$ laser diodes grown by metalorganic chemical vapor deposition. *Appl. Phys. Lett.* **32**, 295–297 (1978).
- Jakubczyk, P., Majchrowski, K. & Tralle, I. Quantum entanglement in double quantum systems and Jaynes-Cummings model. *Nanoscale Res. Lett.* **12**, 236 (2017).
- Ivady, V. et al. Stabilization of point-defect spin qubits by quantum wells. *Nat. Commun.* **10**, 5607 (2019).
- Hwang, H. Y. et al. Emergent phenomena at oxide interfaces. *Nat. Mater.* **11**, 103–113 (2012).
- Odoh, E. O. & Njapba, A. S. A review of semiconductor quantum well devices. *Adv. Phys. Theories Appl.* **46**, 26–32 (2015).
- Schapers, T. *Fabrication of Superconductor/Two-Dimensional-Electron-Gas Structures*. (Springer Berlin Heidelberg, Berlin, Heidelberg, 2001).
- Lin, C.-Y. et al. Orbital-dependent spin textures in Bi_2Se_3 quantum well states. *Phys. Rev. B* **98**, 075149 (2018).
- Benia, H. M. et al. Origin of Rashba splitting in the quantized subbands at the Bi_2Se_3 surface. *Phys. Rev. B* **88**, 081103 (2013).
- Bahramy, M. S. et al. Emergent quantum confinement at topological insulator surfaces. *Nat. Commun.* **3**, 1159 (2012).
- King, P. D. C. et al. Large tunable Rashba spin splitting of a two-dimensional electron gas in Bi_2Se_3 . *Phys. Rev. Lett.* **107**, 096802 (2011).
- Benia, H. M., Lin, C., Kern, K. & Ast, C. R. Reactive chemical doping of the Bi_2Se_3 topological insulator. *Phys. Rev. Lett.* **107**, 177602 (2011).
- Bianchi, M., Hatch, R. C., Mi, J., Iversen, B. B. & Hofmann, P. Simultaneous quantization of bulk conduction and valence states through adsorption of non-magnetic impurities on Bi_2Se_3 . *Phys. Rev. Lett.* **107**, 086802 (2011).
- Datta, S. & Das, B. Electronic analog of the electro-optic modulator. *Appl. Phys. Lett.* **56**, 665–667 (1990).
- Wang, T.-H. & Jeng, H.-T. Wide-range ideal 2D Rashba electron gas with large spin splitting in $\text{Bi}_2\text{Se}_3/\text{MoTe}_2$ heterostructure. *npj Comput. Mater.* **3**, 5 (2017).
- Manchon, A., Koo, H. C., Nitta, J., Frolov, S. M. & Duine, R. A. New perspectives for Rashba spin-orbit coupling. *Nat. Mater.* **14**, 871–882 (2015).
- Bindel, J. R. et al. Probing variations of the Rashba spin-orbit coupling at the nanometre scale. *Nat. Phys.* **12**, 920–925 (2016).

18. Premasiri, K. et al. Tuning Rashba spin-orbit coupling in gated multilayer InSe. *Nano Lett.* **18**, 4403–4408 (2018).
19. Wang, E. et al. Robust gapless surface state and Rashba-splitting bands upon surface deposition of magnetic Cr on Bi₂Se₃. *Nano Lett.* **15**, 2031–2036 (2015).
20. Chen, C. et al. Robustness of topological order and formation of quantum well states in topological insulators exposed to ambient environment. *Proc. Natl. Acad. Sci.* **109**, 3694–3698 (2012).
21. Slomski, B., Landolt, G., Bihlmayer, G., Osterwalder, J. & Dil, J. H. Tuning of the Rashba effect in Pb quantum well states via a variable Schottky barrier. *Sci. Rep.* **3**, 1963 (2013).
22. Koo, H. C. et al. Rashba effect in functional spintronic devices. *Adv. Mater.* **32**, 2002117 (2020).
23. Becker, S., Liebmann, M., Mashoff, T., Prutzer, M. & Morgenstern, M. Scanning tunneling spectroscopy of a dilute two-dimensional electron system exhibiting Rashba spin splitting. *Phys. Rev. B* **81**, 155308 (2010).
24. Papalazarou, E. et al. Unraveling the Dirac fermion dynamics of the bulk-insulating topological system Bi₂Te₂Se. *Phys. Rev. Mater.* **2**, 104202 (2018).
25. Yoshikawa, T. et al. Bidirectional surface photovoltage on a topological insulator. *Phys. Rev. B* **100**, 165311 (2019).
26. Ishida, Y. et al. Emergent photovoltage on SmB₆ surface upon bulk-gap evolution revealed by pump-and-probe photoemission spectroscopy. *Sci. Rep.* **5**, 8160 (2015).
27. Ciocys, S. et al. Manipulating long-lived topological surface photovoltage in bulk-insulating topological insulators Bi₂Se₃ and Bi₂Te₃. *npj Quantum Mater.* **5**, 16 (2020).
28. Neupane, M. et al. Gigantic surface lifetime of an intrinsic topological insulator. *Phys. Rev. Lett.* **115**, 116801 (2015).
29. Zhu, Z.-H. et al. Rashba spin-splitting control at the surface of the topological insulator Bi₂Se₃. *Phys. Rev. Lett.* **107**, 186405 (2011).
30. Bianchi, M. et al. Robust surface doping of Bi₂Se₃ by Rubidium intercalation. *ACS Nano* **6**, 7009–7015 (2012).
31. Wray, L. A. et al. A topological insulator surface under strong Coulomb, magnetic and disorder perturbations. *Nat. Phys.* **7**, 32–37 (2011).
32. Valla, T., Pan, Z.-H., Gardner, D., Lee, Y. S. & Chu, S. Photoemission spectroscopy of magnetic and nonmagnetic impurities on the surface of the Bi₂Se₃ topological insulator. *Phys. Rev. Lett.* **108**, 117601 (2012).
33. Kronik, L. & Shapira, Y. Surface photovoltage phenomena: theory, experiment, and applications. *Surf. Sci. Rep.* **37**, 1–206 (1999).
34. Zhang, Z. & Yates, J. T. Band bending in semiconductors: chemical and physical consequences at surfaces and interfaces. *Chem. Rev.* **112**, 5520–5551 (2012).
35. Tanaka, S.-I. Utility and constraint on the use of pump-probe photoelectron spectroscopy for detecting time-resolved surface photovoltage. *J. Electron Spectros. Relat. Phenom.* **185**, 152–158 (2012).
36. Ulstrup, S. et al. Ramifications of optical pumping on the interpretation of time-resolved photoemission experiments on graphene. *J. Electron Spectros. Relat. Phenom.* **200**, 340–346 (2015).
37. Yang, S.-L., Sobota, J. A., Kirchmann, P. S. & Shen, Z.-X. Electron propagation from a photo-excited surface: implications for time-resolved photoemission. *Appl. Phys. A* **116**, 85–90 (2013).
38. Ciocys, S., Morimoto, T., Moore, J. E. & Lanzara, A. Tracking surface photovoltage dipole geometry in Bi₂Se₃ with time-resolved photoemission. *J. Stat. Mech. Theory Exp.* **2019**, 104008 (2019).
39. Ruda, H. & Shik, A. Surface photovoltage in quantum well structures. *J. Appl. Phys.* **91**, 6476–6480 (2002).
40. Ast, C. R. et al. Local detection of spin-orbit splitting by scanning tunneling spectroscopy. *Phys. Rev. B* **75**, 201401 (2007).
41. Lifshitz, I. Anomalies of electron characteristics of a metal in the high pressure region. *Sov. Phys. JETP* **11**, 1130–1135 (1960).
42. Chen, R., Fan, F., Dittrich, T. & Li, C. Imaging photogenerated charge carriers on surfaces and interfaces of photocatalysts with surface photovoltage microscopy. *Chem. Soc. Rev.* **47**, 8238–8262 (2018).
43. Dittrich, T. & Fengler, S. Surface photovoltage analysis of photoactive materials (World Scientific (Europe), 2020).
44. Gao, Y. et al. Probing of coupling effect induced plasmonic charge accumulation for water oxidation. *Natl. Sci. Rev.* **8**, 6 (2020).
45. Sobota, J. A. et al. Ultrafast electron dynamics in the topological insulator Bi₂Se₃ studied by time-resolved photoemission spectroscopy. *J. Electron Spectros. Relat. Phenom.* **195**, 249–257 (2014).
46. Sobota, J. A. et al. Ultrafast optical excitation of a persistent surface-state population in the topological insulator Bi₂Se₃. *Phys. Rev. Lett.* **108**, 117403 (2012).
47. Jozwiak, C. et al. Spin-polarized surface resonances accompanying topological surface state formation. *Nat. Commun.* **7**, 13143 (2016).
48. Mahajan, A. & Ganguly, S. An analytical model for electron tunneling in triangular quantum wells. *Semicond. Sci. Technol.* **36**, 055012 (2021).
49. Ueno, K. et al. Effective thickness of two-dimensional superconductivity in a tunable triangular quantum well of SrTiO₃. *Phys. Rev. B* **89**, 020508 (2014).
50. Liu, B. et al. Surface roughness scattering in two dimensional electron gas channel. *Appl. Phys. Lett.* **97**, 262111 (2010).
51. Studer, M., Salis, G., Ensslin, K., Driscoll, D. C. & Gossard, A. C. Gate-controlled spin-orbit interaction in a parabolic GaAs/AlGaAs quantum well. *Phys. Rev. Lett.* **103**, 027201 (2009).
52. LaShell, S., McDougall, B. A. & Jensen, E. Spin splitting of an Au(111) surface state band observed with angle resolved photoelectron spectroscopy. *Phys. Rev. Lett.* **77**, 3419–3422 (1996).
53. Shanavas, K. V. & Satpathy, S. Electric field tuning of the Rashba effect in the polar perovskite structures. *Phys. Rev. Lett.* **112**, 086802 (2014).
54. Bychkov, Y. A. & Rashba, E. I. Properties of a 2D electron gas with lifted spectral degeneracy. *JETP Lett.* **39**, 78–83 (1984).
55. Culcer, D., Hwang, E. H., Stanescu, T. D. & Das Sarma, S. Two-dimensional surface charge transport in topological insulators. *Phys. Rev. B* **82**, 155457 (2010).
56. Analytis, J. G. et al. Bulk Fermi surface coexistence with Dirac surface state in Bi₂Se₃: a comparison of photoemission and Shubnikov–de Haas measurements. *Phys. Rev. B* **81**, 205407 (2010).
57. Luttinger, J. M. Fermi surface and some simple equilibrium properties of a system of interacting fermions. *Phys. Rev.* **119**, 1153–1163 (1960).
58. Kuroda, K. et al. Hexagonally deformed Fermi surface of the 3D topological insulator Bi₂Se₃. *Phys. Rev. Lett.* **105**, 076802 (2010).
59. Viol Barbosa, C. E. et al. Direct observation of band bending in the topological insulator Bi₂Se₃. *Phys. Rev. B* **88**, 195128 (2013).
60. Bihlmayer, G., Koroteev, Y., Echenique, P., Chulkov, E. & Blügel, S. The Rashba-effect at metallic surfaces. *Surf. Sci.* **600**, 3888–3891 (2006).
61. Chen, L. et al. Electric-field control of interfacial spin-orbit fields. *Nat. Electron.* **1**, 350–355 (2018).
62. Zhang, Y. et al. Highly efficient electric-field control of giant Rashba spin-orbit coupling in lattice-matched InSb/CdTe heterostructures. *ACS Nano* **14**, 17396–17404 (2020).
63. Bihlmayer, G., Rader, O. & Winkler, R. Focus on the Rashba effect. *N. J. Phys.* **17**, 050202 (2015).
64. Krasovskii, E. E. Microscopic origin of the relativistic splitting of surface states. *Phys. Rev. B* **90**, 115434 (2014).
65. Yuan, L. et al. Uncovering and tailoring hidden Rashba spin-orbit splitting in centrosymmetric crystals. *Nat. Commun.* **10**, 906 (2019).
66. Ereemeev, S. V., Vergniory, M. G., Menshchikova, T. V., Shaposhnikov, A. A. & Chulkov, E. V. The effect of van der Waal's gap expansions on the surface electronic structure of layered topological insulators. *N. J. Phys.* **14**, 113030 (2012).
67. Chenini, L., Aissat, A. & Vilcot, J. Optimization of inter-subband absorption of InGaAsSb/GaAs quantum wells structure. *Superlattices Microstruct.* **129**, 115–123 (2019).
68. Hedayat, H. et al. Non-equilibrium band broadening, gap renormalization and band inversion in black phosphorus. *2D Mater.* **8**, 025020 (2021).
69. Kremer, G. et al. Ultrafast dynamics of the surface photovoltage in potassium-doped black phosphorus. *Phys. Rev. B* **104**, 035125 (2021).
70. Reshchikov, M. A., Foussekis, M. & Baski, A. A. Surface photovoltage in undoped n-type GaN. *J. Appl. Phys.* **107**, 113535 (2010).
71. Sajadi, E. et al. Gate-induced superconductivity in a monolayer topological insulator. *Science* **362**, 922–925 (2018).
72. Matsubara, M. et al. Ultrafast optical tuning of ferromagnetism via the carrier density. *Nat. Commun.* **6**, 6724 (2015).
73. Li, L. J. et al. Controlling many-body states by the electric-field effect in a two-dimensional material. *Nature* **529**, 185–189 (2016).
74. Homid, A. H., Sakr, M. R., Mohamed, A. B. A., Abdel-Aty, M. & Obada, A. S. F. Rashba control to minimize circuit cost of quantum Fourier algorithm in ballistic nanowires. *Phys. Lett. A* **383**, 1247–1254 (2019).
75. Park, S. & Yeyati, A. L. Andreev spin qubits in multichannel Rashba nanowires. *Phys. Rev. B* **96**, 125416 (2017).
76. Smallwood, C. L., Jozwiak, C., Zhang, W. & Lanzara, A. An ultrafast angle-resolved photoemission apparatus for measuring complex materials. *Rev. Sci. Instrum.* **83**, 123904 (2012).
77. Stansbury, C. & Lanzara, A. PyARPES: an analysis framework for multimodal angle-resolved photoemission spectroscopies. *SoftwareX* **11**, 100472 (2020).

ACKNOWLEDGEMENTS

The authors would like to thank Kayla Currier, Daniel Eilbott, Chiu-Yun Lin, Nicholas Dale, and Conrad Stansbury for critical discussions on the experiment and analysis. This work was supported by the Director, Office of Science, Office of Basic Energy Sciences, Materials Sciences and Engineering Division, of the U.S. Department of Energy, under Contract No. DE-AC02-05CH11231, as part of the Ultrafast Materials Science Program (KC2203). The transport work performed by N.M. and J.G.A. was supported by the National Science Foundation under Grant No. 1905397.

AUTHOR CONTRIBUTIONS

S.C. performed the ARPES measurements and the analysis. A.L. and S.C. designed the experiment and contributed to writing the manuscript. N.M. performed the transport measurements and analysis. J.G.A. supported the transport analysis and interpretation.

COMPETING INTERESTS

The authors declare no competing interests.

ADDITIONAL INFORMATION

Supplementary information The online version contains supplementary material available at <https://doi.org/10.1038/s41535-022-00490-2>.

Correspondence and requests for materials should be addressed to Samuel T. Ciocys or Alessandra Lanzara.

Reprints and permission information is available at <http://www.nature.com/reprints>

Publisher's note Springer Nature remains neutral with regard to jurisdictional claims in published maps and institutional affiliations.



Open Access This article is licensed under a Creative Commons Attribution 4.0 International License, which permits use, sharing, adaptation, distribution and reproduction in any medium or format, as long as you give appropriate credit to the original author(s) and the source, provide a link to the Creative Commons license, and indicate if changes were made. The images or other third party material in this article are included in the article's Creative Commons license, unless indicated otherwise in a credit line to the material. If material is not included in the article's Creative Commons license and your intended use is not permitted by statutory regulation or exceeds the permitted use, you will need to obtain permission directly from the copyright holder. To view a copy of this license, visit <http://creativecommons.org/licenses/by/4.0/>.

© The Author(s) 2022